

Further Development of a High-Speed 3-D Density Measurement Technique for Aero-Optics

John Z. Reid¹, Kyle P. Lynch², and Brian S. Thurow³
Auburn University, Auburn, AL 36849

Progress in the development of a 3-D acetone laser induced fluorescence (LIF) technique for aero-optic measurements is reported. Acetone PLIF images were acquired of the turbulent wake of a wall-mounted hemisphere at transonic conditions of approximately Mach 0.78 ($Re_D \approx 9.16 \times 10^5$). The quality of these images was much better than any previous acetone PLIF images acquired of this flow field. An established acetone fluorescence signal model was implemented to convert the images to density field data. Low density cores were visible in many of the images and the density was found to decrease up to 40-50% of the freestream density value in these cores. Acetone PLIF was also attempted with a MHz rate pulse burst laser and high speed camera to acquire time-resolved PLIF images; however, the signal to noise ratio of these images was low and no conclusive information could be obtained. Upgrades to the pulse burst laser system and a new high speed camera will be used in the future to overcome this limitation. These 2-D image studies are critical for development of the 3-D measurement, which is based on the scanning of a laser sheet across the flow. Particle image velocimetry (PIV) was also performed to characterize the flow field and it was found that vorticity fluctuations occur in the turbulent wake and the velocity magnitude ranges from approximately 0-290 m/s. Overall, this work proved that acetone PLIF is a viable technique to calculate density fields in high-velocity, compressible flows (in this case the wake of a hemisphere which closely resembles the flow over a turret mounted to an aircraft). In addition, the results from the experiments better characterized this flow field and provided valuable information in regard to the extent of the density fluctuations and what needs to be modified in order to achieve 3-D acetone LIF. This is valuable information as progress is made toward 3-D acetone LIF density measurements which will enable calculation of aero-optic distortion.

I. Introduction

The propagation of a collimated, coherent beam of light is dependent on the index-of-refraction of the medium through which it travels. In turbulent flow fields, density fluctuations directly lead to fluctuations in the index of refraction, causing the wavefront of the beam to become aberrated. The interaction of fluid properties and light propagation is termed "aero-optics." This research field has attracted interest recently as imaging, optical communications,

¹ Graduate Research Assistant

² Graduate Research Assistant

³ Associate Professor, corresponding author: thurow@auburn.edu

and directed energy weapon systems have become more common. In each of these cases, degradation of the optical wavefront places a limit on the performance of these systems, particularly when used on aircraft platforms. An example is a turret-mounted laser aperture on the fuselage of an aircraft; the turbulent boundary layer, necklace/horseshoe vortex, separated shear layer, and turbulent wake generate large density fluctuations that alter the wavefront as the beam exits the aperture. As the beam continues towards a target, the distorted wavefront causes the beam to diverge and degrade in quality. By the time the beam reaches the target, it has lost its initial coherence and is less effective.

Quantitatively, the distortion of an optical wavefront can be described by variations in the optical path length (OPL). The OPL is calculated by an integration of the three-dimensional index of refraction in the direction of light propagation, z , as seen in Eqn. 1:

$$OPL(x, y, t) = \int n(x, y, z, t) dz \quad (1)$$

The relation between index of refraction and density is dependent on the fluid. In the case of air, Eqn. 2 is used, where the Gladstone constant K is $2.23 \times 10^{-4} \text{ m}^3/\text{kg}$ for air.

$$n = 1 + K\rho \quad (2)$$

Thus, the distortion of an optical wavefront is the integrated effect of the three-dimensional density (index-of-refraction) field through which the beam passes. In principle, if the three-dimensional density field of the flow is known, adaptive optics can be used to correct for the distortion. However, correction for aero-optic distortion is beyond the scope of this work.

In turbulent flow fields, the flow structures causing density fluctuations are highly three-dimensional. Therefore, it is necessary to develop a 3-D diagnostic technique that can determine the density at each point in the flow field through which a beam travels. Conventional flow diagnostics are unable to make 3-D density measurements; nonetheless, past investigations have succeeded in using a variety of experimental methods to characterize various turbulent flows and resulting wavefront aberrations¹⁻⁷. These studies have found that in addition to compressibility effects, the unsteady behavior of the large scale turbulence structures in the flow is a dominant source of distortion. These large-scale vortical structures produce low pressure wells at their core, causing a change in density throughout the structure^{8,9}. While these findings have increased the understanding of some basic mechanisms of distortion, fully quantifying these effects and designing optimal flow control or adaptive optics techniques requires the development of a technique for measuring the 3-D density field.

A number of efforts have been made over the years to develop 3-D flow measurement systems, including stereographic¹⁰, holographic^{11,12}, tomographic¹³, and laser sheet scanning¹⁴ methods. In principle, stereographic-, holographic-, and tomographic- based techniques are capable of acquiring instantaneous three-dimensional flow data, but are generally restricted to particle-based measurements and have numerous other restrictions that restrict their application to specialized scenarios. Therefore, the approach that is adopted in this effort is laser sheet scanning. In this technique, a laser beam is formed into a thin sheet using a cylindrical lens and is scanned through the flow field using a high-speed scanning mirror. As the laser sheet passes through the flow field, a sequence of images at different planes throughout the flow field is acquired. Three-dimensional field data can then be reconstructed from the stack of 2-D images.

An advantage to laser sheet scanning is that it is an extension of traditional planar diagnostic techniques. For measuring density, planar laser induced fluorescence (PLIF) is widely used and is well understood¹⁵. By extending PLIF, in the case of this work acetone PLIF, with laser sheet scanning, a 3-D density field can be obtained. The pulse burst laser system (see Sec. III.D.) and high speed cameras at Auburn University are capable of producing laser pulses and capturing images at MHz rates, allowing the technique to be used for high-speed flows. However, before 3-D acetone LIF can be performed using laser sheet scanning, acetone PLIF must be proven as a viable technique to acquire 2-D density field data for a single plane in high velocity, compressible flow fields in a wind tunnel.

This paper presents progress in the development of a high-speed 3-D density measurement technique using acetone PLIF. In particular this paper shows that high resolution acetone PLIF images can be obtained for a high-velocity, compressible flow (in this case the wake of a hemisphere which closely resembles the flow over a turret mounted to an aircraft) and converted to density field data using an established acetone fluorescence signal model. Additionally, this paper presents attempts made to obtain high-speed, time-resolved acetone PLIF images. The ability to obtain high-speed acetone PLIF images must be proven before the technique can be extended to 3-D through laser sheet scanning. An explanation of an upgrade of the pulse burst laser system to improve signal levels is presented, along with new high speed cameras that will be used in future studies to increase signal to noise ratio. PIV data of the flow field is also presented and compared to acetone PLIF density data obtained for this flow field.

II. Acetone LIF Development

A. Background of Acetone LIF

LIF is based on the absorption and fluorescence of laser light by molecules either already present or artificially introduced into a flow field. The chemical characteristics of particular molecules results in unique absorption spectra, typically in the ultraviolet (UV). Using an appropriate light source with strong spectral overlap, light can be efficiently absorbed by the molecule, raising its energy level. To return to an equilibrium state, both short-term (fluorescence) and long-term (phosphorescence) radiative processes occur, emitting photons within separate, longer-wavelength emission spectra. Acetone was chosen as the tracer molecule for this work because of the favorable characteristics it possesses, which include low cost, safe handling characteristics, and broadband absorption spectrum, which peaks from 260 to 290 nm. Thus, acetone could be strongly excited by converting efficient Nd:YAG laser systems to their fourth-harmonic output at 266 nm. The fluorescence emission is also broadband and peaks from 445 to 480 nm, a range of wavelengths efficiently detected by CCD sensors. For acetone PLIF, a 266 nm laser sheet passes through the flow field of interest, the acetone molecules absorb the 266 nm light, and a fraction of the acetone molecules fluoresce. The fluorescence of the acetone molecules is captured on a CCD. The normalized fluorescence signal can be correlated to a density value, allowing a 2-D density field to be calculated from an acetone PLIF image.

The photophysics and physical qualities of acetone have been well characterized by Lozano et al.¹⁶; in particular, the weak dependence of fluorescence signal on pressure and temperature and the quenching of the long-lifetime phosphorescence signal by atmospheric oxygen were reported. Further work by Thurber¹⁷ succeeded in establishing a fluorescence quantum yield model where changes in temperature, pressure, wavelength, and bath gas were

investigated to determine their effect on fluorescence quantum yield. Thurber also obtained the absorption cross-section values of acetone for a wide-range of temperatures. Both fluorescence quantum yield and absorption cross-section play an important role in the fluorescence signal equation for acetone explained below. This fluorescence signal equation can be simplified and used to find the density throughout the flow field. These findings have established acetone as a suitable molecular tracer for accurate measurements in fluids.

B. Acetone Fluorescence Signal Model

The acetone fluorescence signal equation¹⁷ is shown below in Eqn. 3:

$$S_f = \frac{E}{hc/\lambda} \eta_{opt} dV_c \left[\frac{\chi_{acetone} P}{kT} \right] \sigma(\lambda, T) \phi(\lambda, T, P, \sum_i \chi_i) \quad (3)$$

Where E is the laser fluence, hc/λ is the energy of a photon at the excitation wavelength λ , η_{opt} represents the overall efficiency of collection optics, and dV_c is the collection volume. The bracketed term is the acetone number density, given as a product of acetone mole fraction $\chi_{acetone}$ and total pressure P divided by the Boltzmann constant k times temperature T . The final two terms are functional relations; σ is the molecular absorption cross-section of the tracer molecule and ϕ is the fluorescence quantum yield.

This generalized signal equation can be simplified for an analysis of how the signal level varies with changes in flow density. An assumption made is that the acetone mole fraction is approximately constant and uniform entering the test section. This is accomplished in experiments by seeding the acetone into the flow far upstream of the stagnation chamber, allowing for dispersal and evaporation prior to entering the test section. Using this assumption and ignoring constant terms, the signal equation can be reduced to Eqn. 4.

$$S_f^+ \propto \rho \sigma(T) \phi(T, P) \quad (4)$$

Eqn. 4 establishes a relationship between the thermodynamic properties of the gas and the fluorescent signal. This signal is directly proportional to the flow density with a weak, but non-negligible dependence on temperature as indicated in the absorption cross-section and fluorescence quantum yield terms. Pressure also plays a role; however, its effect can be directly tied to the density and temperature through the equation of state. Fortunately, Thurber developed a fluorescence yield model that takes into account wavelength, pressure, temperature, and bath gas, allowing the value of fluorescence yield to be calculated across a range of conditions. The bath gas is an important aspect because if oxygen is present in the bath gas, slight quenching of the fluorescence occurs. Also, the absorption cross-section relationship vs. temperature can be interpolated.

For the measurements described herein, it is not practical to make an absolute measure of the signal as described in Eqn. 3. Instead, one can take advantage of the fact that the thermodynamic properties of the flow are a known quantity in the free stream. This allows an estimate of the flow density to be made by looking at the ratio in signal between an arbitrary point in the flow and the free stream, as shown in Eqn. 5:

$$\frac{S_f}{S_{f_\infty}} = \frac{\rho\sigma(T)\phi(T,P)}{\rho_\infty\sigma(T)_\infty\phi(T,P)_\infty} \quad (5)$$

Eqn. 5 essentially describes an in-situ calibration where the free stream flow is used to calibrate unknown or undetermined quantities, such as laser fluence and optical collection efficiency. As will be discussed later in detail, determination of a density value depends on the estimate of the temperature at any given point such that the value for the absorption cross-section and fluorescent yield can be determined. In the absence of an independent temperature measurement, a bound is placed on these values. It is found that the variation of absorption cross-section and fluorescence quantum yield with temperature is relatively weak, but non-negligible. This is discussed further in Sec. IV.

III. Experimental Arrangement

To facilitate the development of the high-speed 3-D density measurement technique and provide a relevant flow field for aero-optic studies, a small-scale transonic wind tunnel was designed and constructed. A hemisphere, which possesses similar qualities to a turret mounted on an aircraft, is mounted to the wall of the test section to generate a flow field with substantial density gradients and three-dimensional flow structures, including a flat plate boundary layer, a necklace/horseshoe vortex that wraps around the base of the hemisphere, a shear layer, shedding vortices, and a turbulent wake. Shock waves can also form at approximately 90° from the horizontal. To characterize the performance of the tunnel and the structure of the flow field, Schlieren imaging and 2-D particle image velocimetry (PIV) experiments were performed. These experiments showed regions of density fluctuations and vorticity fluctuations. In addition, acetone PLIF experiments were performed.

A. Transonic Wind Tunnel and Model Geometry

A fixed wall transonic wind tunnel was specifically designed to investigate the flow over a hemisphere (particularly the turbulent wake region) at or near transonic conditions. The transonic wind tunnel cross section is approximately 4" x 4" and has optical access on three sides. All three optical windows are UV-fused silica, but the bottom window also has an anti-reflective (AR) coating specifically for 266nm and 532nm light. The bottom window is AR coated for passage of the 266 nm laser sheet (acetone PLIF experiments) and the 532 nm laser sheet (PIV experiments). The compressed air source is an Ingersoll-Rand compressor equipped with a dessicate air dryer, capable of providing 650 cfm of air at pressures up to approximately 125 psig. The compressed air is stored in two large tanks that are connected to the stagnation chamber using large diameter compressed air lines. As seen in Figure 1, the stagnation chamber is attached to a smooth contour nozzle followed by the test section, the diffuser, and a 90° elbow where the flow exits the laboratory. Just downstream of the test section is a plate with a slight bump that creates a cross sectional area, A^* (throat area), which is slightly smaller than the cross sectional area of the test section, A . The flow is choked at A^* and through the ratio A/A^* , transonic conditions are forced in the test section (approximately Mach 0.78 flow). The advantage to this design is that the Mach number is held constant for longer periods of time as the upstream pressure in the storage tanks drops. One disadvantage, however, is a time-

dependent drop in the test section static pressure over the course of a single run. These pressures are monitored and recorded over the course of a run such that the tunnel conditions are known. The model is a 1 inch diameter hemisphere that is mounted to the ceiling of the wind tunnel, approximately 4 inches downstream from the beginning of the test section. It is constructed of aluminum and is anodized black.

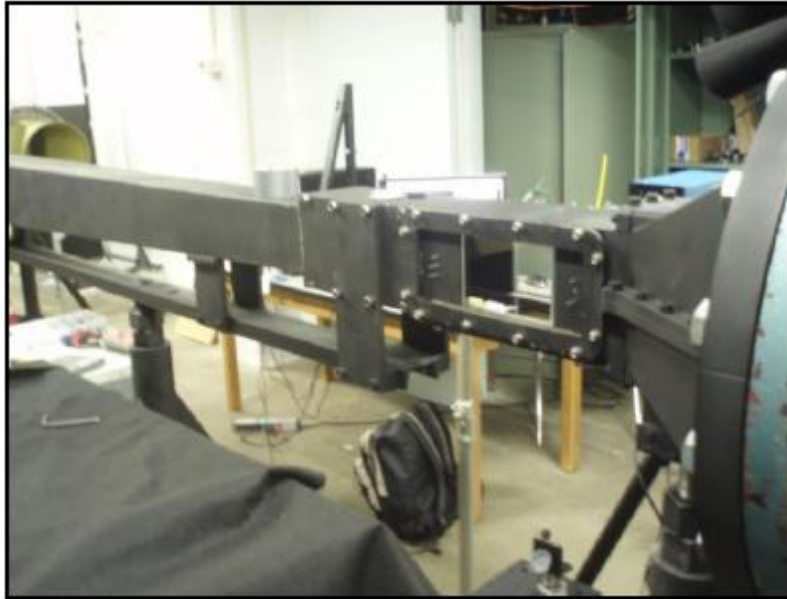


Figure 1: Transonic wind tunnel

The wind tunnel had the ability to be seeded for two different types of experiments. A nitrogen tank pressurizes a small pressure vessel that contains liquid acetone. An EPDM hose, submerged in the liquid acetone, is attached to an exit pipe, a solenoid valve, a wall fitting, and a spray nozzle. The spray nozzle is connected to a wall fitting that is connected through the wall of the compressed air supply line far upstream of the test section of the wind tunnel. During testing, the small pressure vessel is pressurized and the solenoid valve is opened, allowing the liquid acetone to be injected into the compressed air supply line. The spray nozzle is oriented in the upstream direction. This assists in dispersion of the liquid acetone and helps ensure that the liquid acetone evaporates before entering the test section, so only acetone vapor and air are in the test section. A schematic of this seeding setup is shown in Figure 2. For PIV experiments, alumina particles are seeded far upstream of the test section of the wind tunnel using a method similar to that described by J.H. Wernet and M.P. Wernet¹⁸. This seeding is performed the same way as for acetone PLIF experiments except alumina particles (Sumitomo AKP-20) of approximately 0.5 μm diameter are mixed with acetone and then added to the pressure vessel. When the acetone evaporates, only alumina particles, acetone vapor, and air enter the test section. Thus, the 532 nm laser sheet used for PIV can only scatter off of the alumina particles. This seeding setup also presents the opportunity to perform simultaneous PIV and acetone PLIF experiments in the future.

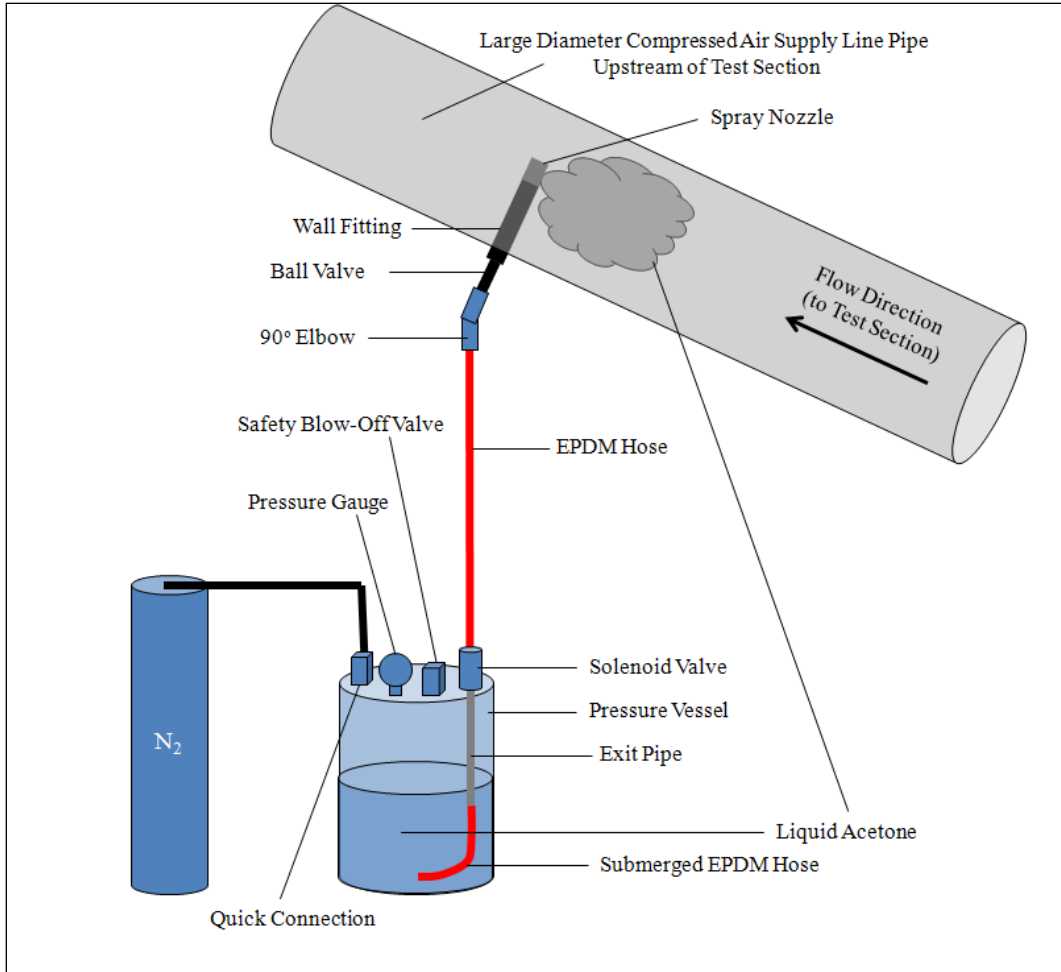


Figure 2: Schematic of seeding system used for acetone PLIF and PIV experiments. For acetone PLIF, only acetone was used. For PIV, alumina particles were mixed with acetone.

B. PIV Setup

In order to provide quantitative information for the flow field, PIV experiments were performed along the centerline of the test section. For PIV illumination, a New Wave Research Solo III PIV laser was used, capable of producing 50 mJ/pulse. Using a combination of spherical lenses and a cylindrical lens, a thin 532nm laser sheet was formed and directed upward through the bottom window of the test section along the centerline of the test section. The pH of the liquid acetone/alumina particle mixture, which can influence the quality of the suspension, was not measured.

The signal scattered by the alumina particles was captured using a Cooke Corp. Sencicam QE camera. A 25 mm focal length lens was used for imaging, allowing a field of view approximately 93 mm x 50 mm with resolution 1376px x 736 px (the camera is capable of 1376px x 1040px, but the pertinent data existed over a small vertical area and a large horizontal area of the field of view. Thus only 1376 px x 736 px were used). The spatial resolution of the

individual images was approximately $67 \mu\text{m}/\text{px}$. The interpulse timing with this field of view was $2 \mu\text{sec}$.

C. Acetone PLIF Setup

High resolution, low image acquisition speed acetone PLIF experiments were performed near the centerline of the test section. Illumination for these experiments was provided by the PIV laser explained above, except an externally mounted KDP crystal was used to convert the 532 nm light to 266 nm light. After harmonic conversion, a thin 266 nm laser sheet was formed using a cylindrical lens and directed upward through the bottom window of the test section, as seen in Figure 3. The laser sheet was approximately 2 inches wide and $0.5\text{-}1 \text{ mm}$ thick. The pulse energy was approximately $22 \text{ mJ}/\text{pulse}$, obtained by using both laser heads with a 100 nsec separation. Images were obtained slightly off the centerline ($<1/8 \text{ in}$ because of a light scattering problem on the centerline) of the test section with the Sensicam QE unintensified camera using 2×2 binning. A 25 mm lens was used with $f\#1.4$, giving a field of view of approximately $35.9 \text{ mm} \times 27.1 \text{ mm}$ with a resolution of $688 \text{ px} \times 520 \text{ px}$ (only $500 \text{ px} \times 520 \text{ px}$ was useful data, so the actual field of view was approximately $26.1 \text{ mm} \times 27.1 \text{ mm}$). The spatial resolution of the images was approximately $52 \lambda\text{m}/\text{px}$.

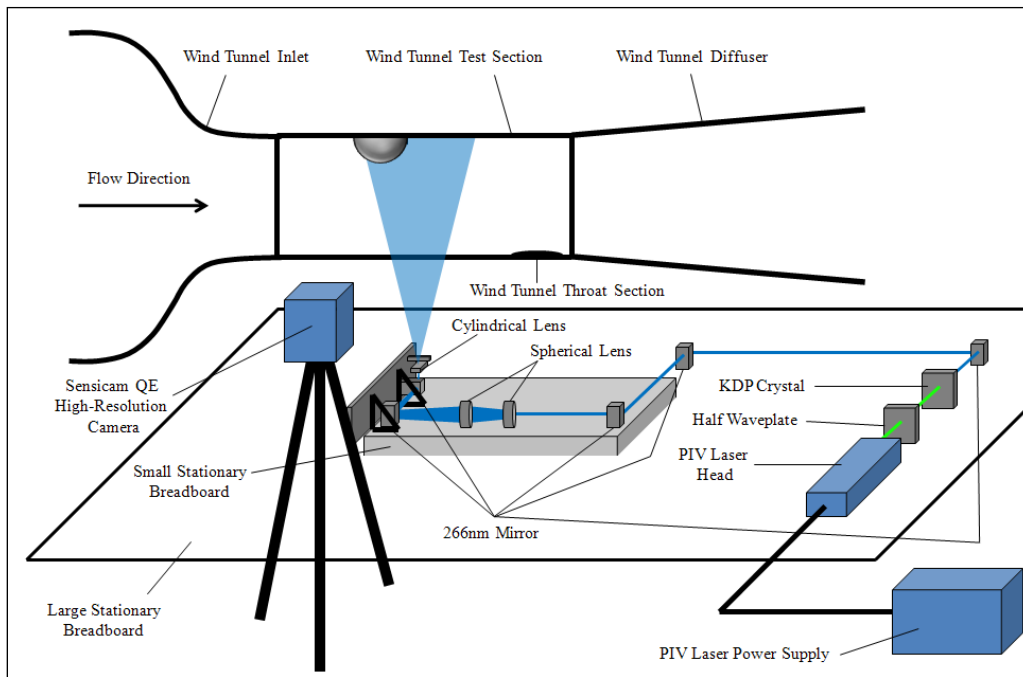


Figure 3: Schematic of acetone PLIF experimental setup

D. Time-resolved Acetone PLIF Setup

Time-resolved acetone PLIF experiments were attempted using the same optics as single-shot PLIF, but using a pulse burst laser and DRS Hadland Ultra68 camera. The pulse burst laser that was used in these experiments was a 3rd-generation design based on an initial design by Wu et. al.¹⁹, a 2nd-generation design by Thurow et. al.²⁰, and similar 2nd-generation systems in place

elsewhere^{21,22}. A thorough description of the design features and performance has been reported previously²³, however a brief overview of the system is provided here, with emphasis on the conversion process to yield 266 nm light.

The configuration of the system is classified a master oscillator power amplifier (MOPA), where a burst of low energy pulses is formed and amplified through a chain of power amplifiers. The master oscillator of the system is a low power (100 mW) continuous-wave Nd:YAG laser operating at 1064 nm, which is “sliced” into a configurable burst of pulses using an Acousto-Optic Modulator (AOM). This device is capable of creating an arbitrary number of pulses, as short as 20 nsec each, with a maximum repetition rate of over 10 MHz, and with contrast ratios of over 2,000:1.

The resulting short, low energy pulses (1 nJ/pulse) enter a series of five flashlamp-pumped Nd:YAG rod amplifiers, with rod diameters of 4, 5, 6.3, 9.5, and 12.7 mm, respectively. The first three amplifiers operate in a double-pass configuration for maximum gain while in the small to moderate signal regime. The final two amplifiers are single-passed to minimize gain depletion throughout the duration of the pulse burst. Faraday isolators are placed between each amplifier stage to reduce gain depletion through parasitic oscillation in the system. Figure 4 is an image of the master oscillator and power amplifier chain. After amplification, the high energy pulses (70 mJ/pulse at 1064 nm) are frequency doubled to 532 nm (green) by use of an 8 mm x 8 mm x 10 mm KTP nonlinear crystal. This conversion yielded 20 mJ/pulse, corresponding to a 28% conversion efficiency. To further generate light at 266 nm, a similar harmonic conversion process is used with Type I BBO. BBO has been found to work more efficiently than KDP when used with the pulse burst laser, which allows for better collimation and longer coherence lengths than the PIV laser used in the single-shot acetone PLIF studies. This conversion process yielded 4 mJ/pulse, corresponding to a 20% conversion efficiency.

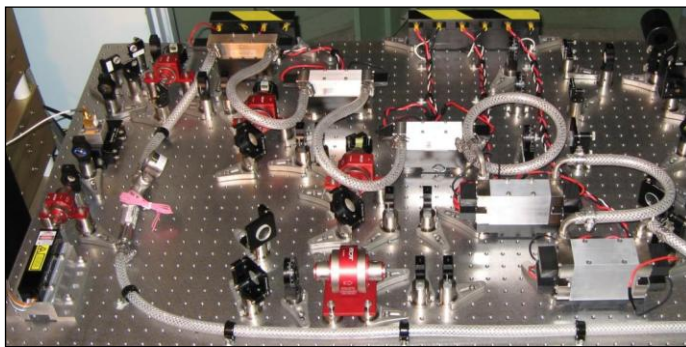


Figure 4: Photograph of pulse burst laser system with five amplifiers

A DRS Hadland Ultra68 high-speed camera was used for capturing fluorescence images. It is capable of acquiring 68 images at up to 500,000 frames per second, with an individual image resolution of 220 x 220 pixels. Thus, an entire image sequence takes 136 μ sec to acquire. Due to the intensified nature of the camera, the noise characteristics are unfavorable, with variations in flat field intensity values being around 10%. Additionally, the design of the camera uses a number of beamsplitters, which further degrades the signal levels and introduces slight spatial positioning jitters in each frame that must be corrected after acquisition. Both of these issues limit the utility of the camera in this study.

IV. Experimental Results

The flow field information obtained from these experiments was analyzed and the general flow field structure was compared to information found in literature to confirm behavior that is consistent with expectations. Furthermore, the PIV data was compared to the PLIF data to identify areas of the flow marked by stronger turbulent features.

A. Results from PIV Experiments

Single-shot PIV image pairs were obtained for this flow field along the centerline and were processed with PIVPROC v.7.02 software provided by NASA. This software incorporates a multi-pass cross-correlation scheme with the window deformation technique²⁴. Correlation window sizes of 32 x 32 pixels were used with a 50% overlap. The results were single image pair velocity vectors for this flow field.

By obtaining the velocity vectors for a single-shot PIV image pair for this flow field, the vorticity field could be calculated. Instantaneous vorticity and velocity magnitude plots are provided from the PIV experiments along the centerline in Figures 5 and 6, respectively. As seen in Figure 5, there are regions of high positive and high negative vorticity in the turbulent wake. In Figure 6 it is seen that the highest velocity magnitude is approximately 290 m/s and occurs in the shear layer. The low velocity magnitudes occur in the turbulent wake and just in front of the hemisphere. It is also seen in Figure 6 that stagnation points (the velocity magnitude is zero) exist on the front and back of the hemisphere where the hemisphere meets the wall.

The velocity magnitude data obtained is useful because it can be used to calculate approximate Mach numbers and Reynolds numbers in the flow field. The freestream velocity magnitude is 240-260 m/s, taken as 250 m/s for calculation purposes, and the shear layer velocity magnitude is 290 m/s. If $M = \frac{V}{A} = \frac{V}{\sqrt{\gamma RT}}$ is plugged into the isentropic $\frac{T_o}{T} = 1 + \frac{\gamma-1}{2} M^2$

equation and the resulting equation is solved for T, then $T = T_o - \frac{\gamma-1}{2} \frac{V^2}{\gamma R}$. Using $T_o=300$ K and

$V_{\text{shearlayer}}=290$ m/s, $T_{\text{shearlayer}}$ is approximately 258.14 K. Using $T_o=300$ K and $V_{\lambda}=250$ m/s, T_{λ} is approximately 268.89 K. If these values of T are used with their corresponding values of V in the Mach number equation, then the Mach numbers are approximately $M_{\text{shearlayer}}=0.9$ and $M_{\lambda}=0.76$. This freestream Mach number is close to the approximate freestream Mach number of 0.78 found from P_o/P during testing. Using the isentropic relations with the freestream temperature value calculated and stagnation condition values, the density of the freestream can be approximated. In addition, the dynamic viscosity can be approximated at the calculated freestream temperature. These values can be used to calculate the freestream Reynolds number of $Re_D=916,000$.

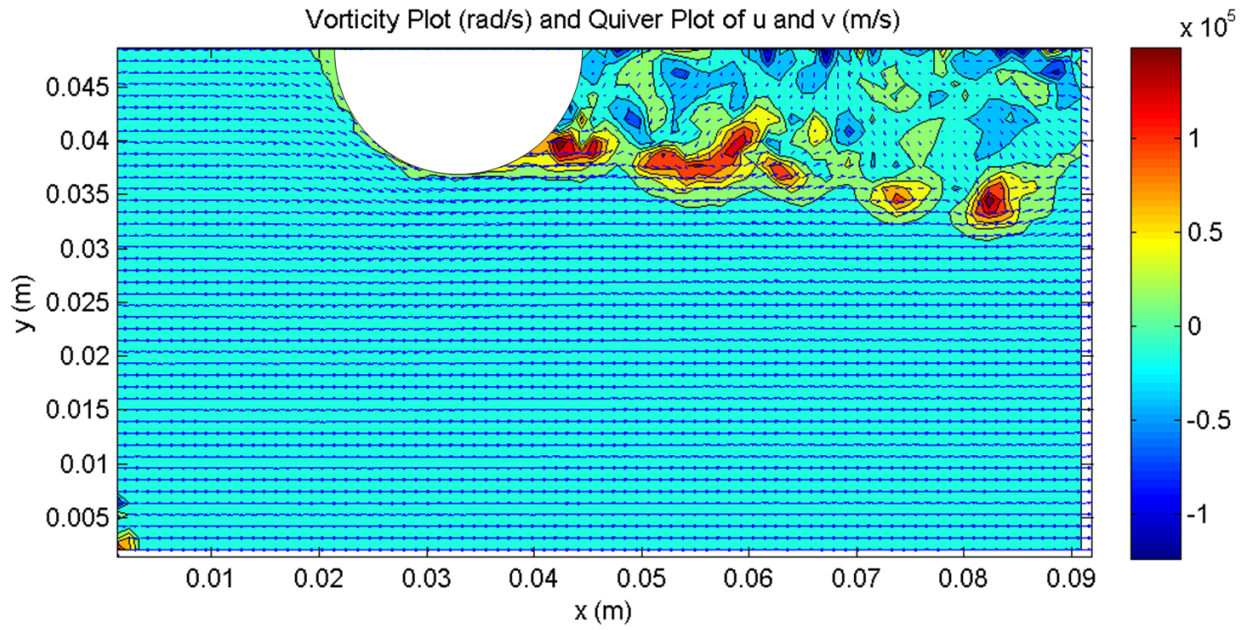


Figure 5: Plot of vorticity (rad/s) and overlapping quiver plot of u and v (m/s) for single image pair on centerline

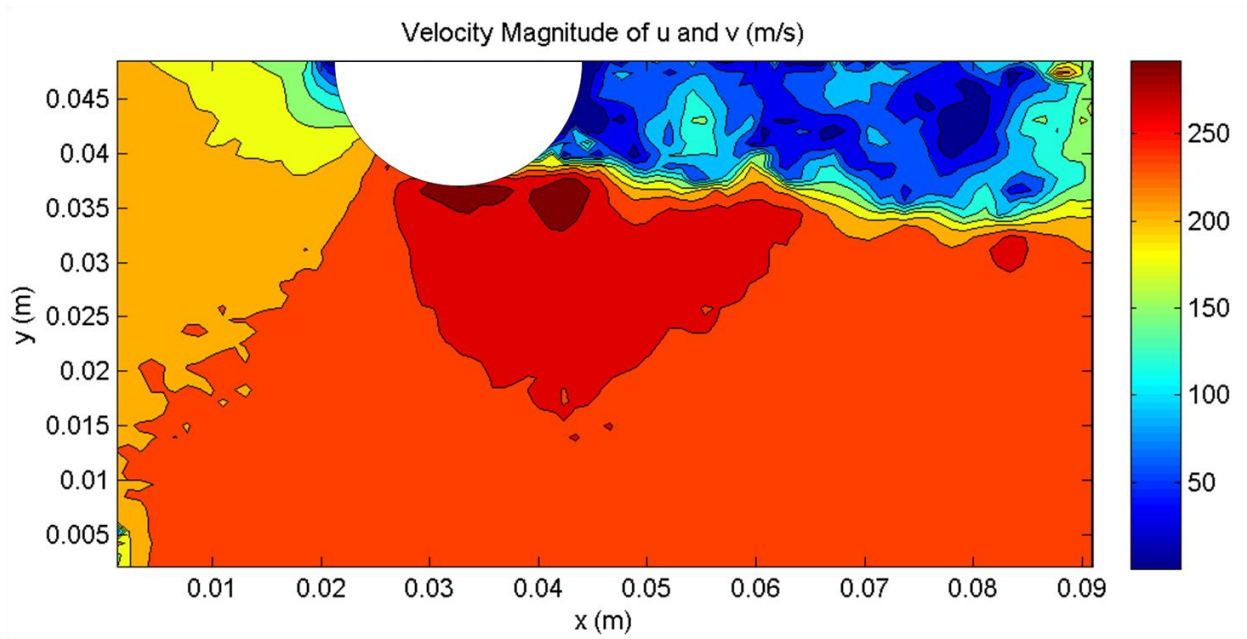


Figure 6: Plot of velocity magnitude of u and v (m/s) for single image pair on centerline

B. Results from PLIF Experiments

1) Image Processing

After acetone PLIF images were obtained, an average dark image was subtracted from each image. A trapezoidal laser sheet normalization correction was then applied to each image. This correction is necessary to account for variations in the incident laser sheet intensity across the width of the imaging region. The correction process also accounts for the fact that the laser sheet, formed by a cylindrical lens, is spreading as it passes through the test section. As such, the image coordinates (x,y) are mapped to a set of cylindrical coordinates (r,θ) using a virtual origin for the laser sheet that is obtained through trial and error. A set of correction coefficients vs. θ is then extracted by examining the intensity of the image that corresponds to the free stream flow. The idea is that far from the hemisphere, the density and temperature should be constant and, therefore, the image intensity should also be constant. Any variations in image intensity must therefore be due to variations in the incident light sheet intensity. In essence, the signal and density ratio in Eqn. 5 is being forced to equal 1.0. Assuming that the laser sheet intensity is constant for constant θ , all points in the image are corrected by interpolating the correction coefficients for the exact angle of each point. The intensity at each point is then multiplied by the corresponding correction coefficient for that point. Each image was then normalized by its average freestream intensity value. The decrease in laser intensity with increasing r was not accounted for as the change in r was relatively small. The end result was an image ratio where

the value at each pixel corresponds to the normalized signal, $\frac{S_f}{S_{f_\infty}}$, indicated in Eqn. 5. These values were then converted to a density value using a calibration curve as described in the next section.

2) Calibration Curves

As discussed earlier, one must model the temperature of the flow field in order to determine the density from the signal ratio. The temperature is necessary to estimate the local values of the absorption cross-section and fluorescence quantum yield because they are both a function of temperature. To estimate fluorescence quantum yield, the fluorescence quantum yield model described in Thurber was used, assuming air as the bath gas. Absorption cross-section was found by interpolating absorption cross-section vs. temperature data from Thurber. It is important to note that the dependence of the fluorescence quantum yield on pressure is redundant in this case as the equation of state can be used to relate the density, temperature, and pressure. Thus, one only needs to estimate temperature to determine a calibration curve of normalized acetone fluorescence signal vs. normalized density.

In these acetone PLIF experiments, the temperature is an unknown. As such, it was desired to model the influence of temperature on the measurement accuracy. To do so, the upper and lower bounds on the temperatures that might be realized in the flow were considered. Assuming adiabatic flow, it was deemed reasonable to assume that the maximum temperature the flow would obtain in the near wake would be equal to the stagnation temperature, T_o , which was taken here as 300 K (room temperature). On the other end of the spectrum, it should be recognized that as the flow isentropically expands around the hemisphere, the local Mach number can approach and exceed Mach 1.0, thus leading to an associated temperature drop. As explained in IV.A., the shear layer Mach number was found to be approximately 0.9. Therefore,

placing a boundary of Mach 1.0 flow was deemed to be a safe estimate and placed a lower bound on the temperature of approximately 250 K. Thus, it was assumed that the temperature varies between 250 and 300 K in this flow field.

Figure 7 shows the calibration curve for three cases: (1) $T = T_{\min} = 250$ K, (2) $T = T_{\max} = 300$ K, and (3) $T = T_{\infty} (\rho/\rho_{\infty})^{\gamma-1}$. The last case corresponds to an assumption of isentropic expansion and serves as a point of reference. T_{∞} and P_{∞} were calculated with the isentropic relations using the stagnation conditions and $M=0.78$ (as opposed to section IV.A. which calculated/estimated a freestream Mach number of 0.76 based upon PIV data from one image pair). Then λ_{∞} was calculated from T_{∞} and P_{∞} . As can be seen in Figure 7, all three curves show that the signal increases approximately linearly with flow density with only a slight dependence on the local temperature. Still, it can be seen that temperature does have an influence that

restricts the accuracy of the measurements. It was found that from approximately $\frac{S_f}{S_{f_{\infty}}} = 0.4-1.46$

the maximum percent difference in the normalized density values calculated (for a particular normalized signal value) from one calibration curve to another is approximately 8%. This is clearly seen in Figure 8 which plots percent difference in normalized density value calculated vs. normalized signal. The percentdiffTisenTmax curve, for example, is the percent difference between density values calculated using the isentropic curve and the $T=T_{\max}$ curve at specific

normalized signal values. The maximum of 8% percent difference occurs at approximately $\frac{S_f}{S_{f_{\infty}}}$

$=0.4$, which corresponds to $\lambda/\lambda_{\lambda}$ of approximately 0.45-0.50. In the final single shot density images, shown in Sec. IV.B.3), the maximum density drops from the freestream density are near 40-50%, thus this 8% is a reasonable bound for the percent difference in the results obtained by using different curves. For the aero-optic application of this work, where we are interested in the integrated density along a path and local changes in density, it remains to be seen how important this accuracy will be. This is a topic we plan on exploring in the near future.

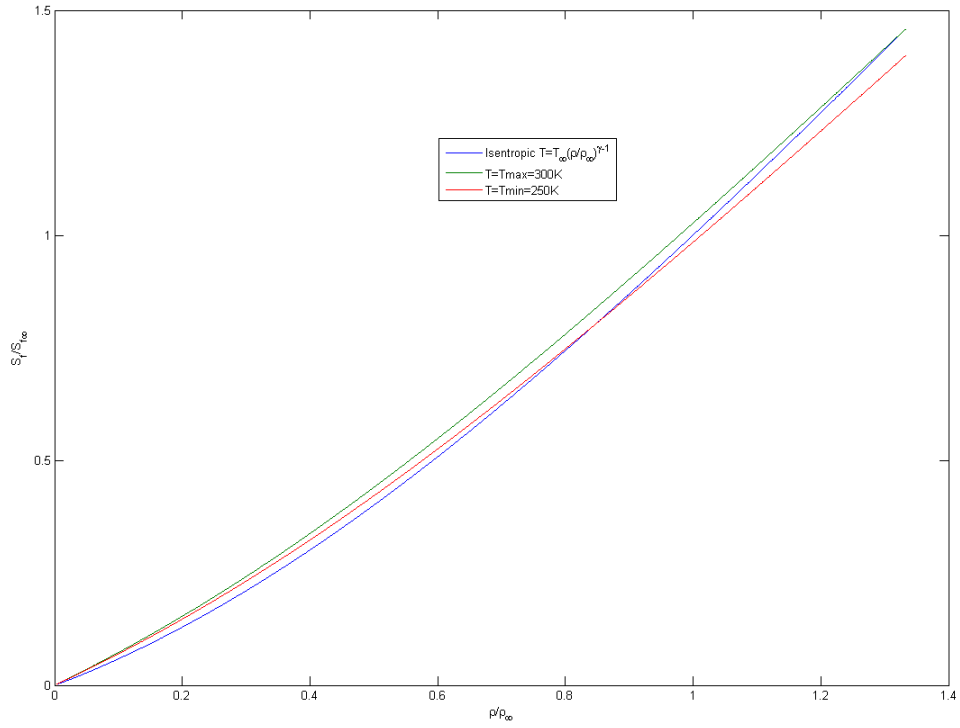


Figure 7: Calibration curves

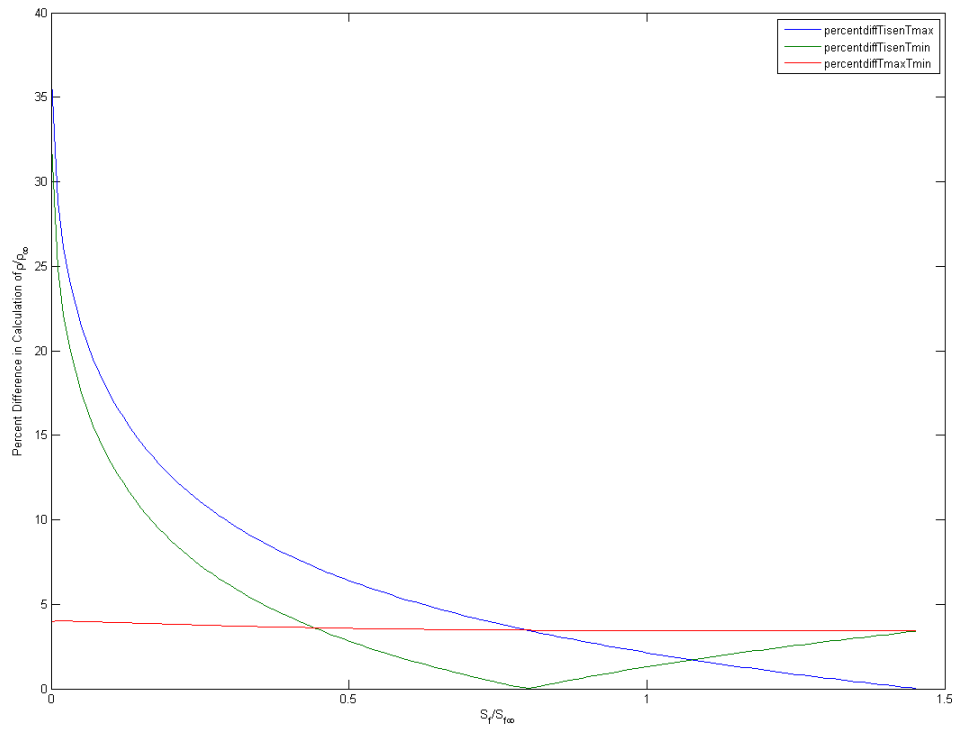


Figure 8: Percent difference in λ/λ_λ values calculated (for a specific value of $\frac{S_f}{S_{f\infty}}$) from one calibration curve to another

3) Corrected Images and Density Values

The isentropic calibration curve was used to calculate the density values for the images presented in this paper. Density data was found for 70 corrected single shot acetone PLIF images. These 70 images were averaged and additionally a standard deviation plot was created for these images. The turbulent wake is visible in the single shot density images, as seen in Figure 8 (the gray colorbar in this plot is normalized density λ/λ_λ). Large density fluctuations clearly occur in the turbulent wake region. This is where large vorticity fluctuations occur as well, as evidenced by the PIV experiments. These images show that in the shear layer and wake for the most part the density drops from the freestream density are 20-25%. However, at specific points in the shear layer and wake, density drops of 40-50% of the freestream density are seen. The average density image, as seen in Figure 9, shows that in the shear layer and turbulent wake the maximum density drop from the freestream density is approximately 20-25%. This proves that an individual image is a true representation of the extent of these density fluctuations and an average image is not. The standard deviation plot, as seen in Figure 10, shows that the maximum standard deviation of approximately $\lambda/\lambda_\lambda 0.1-0.15$ occurs in the shear layer region and the upper portion of the wake.

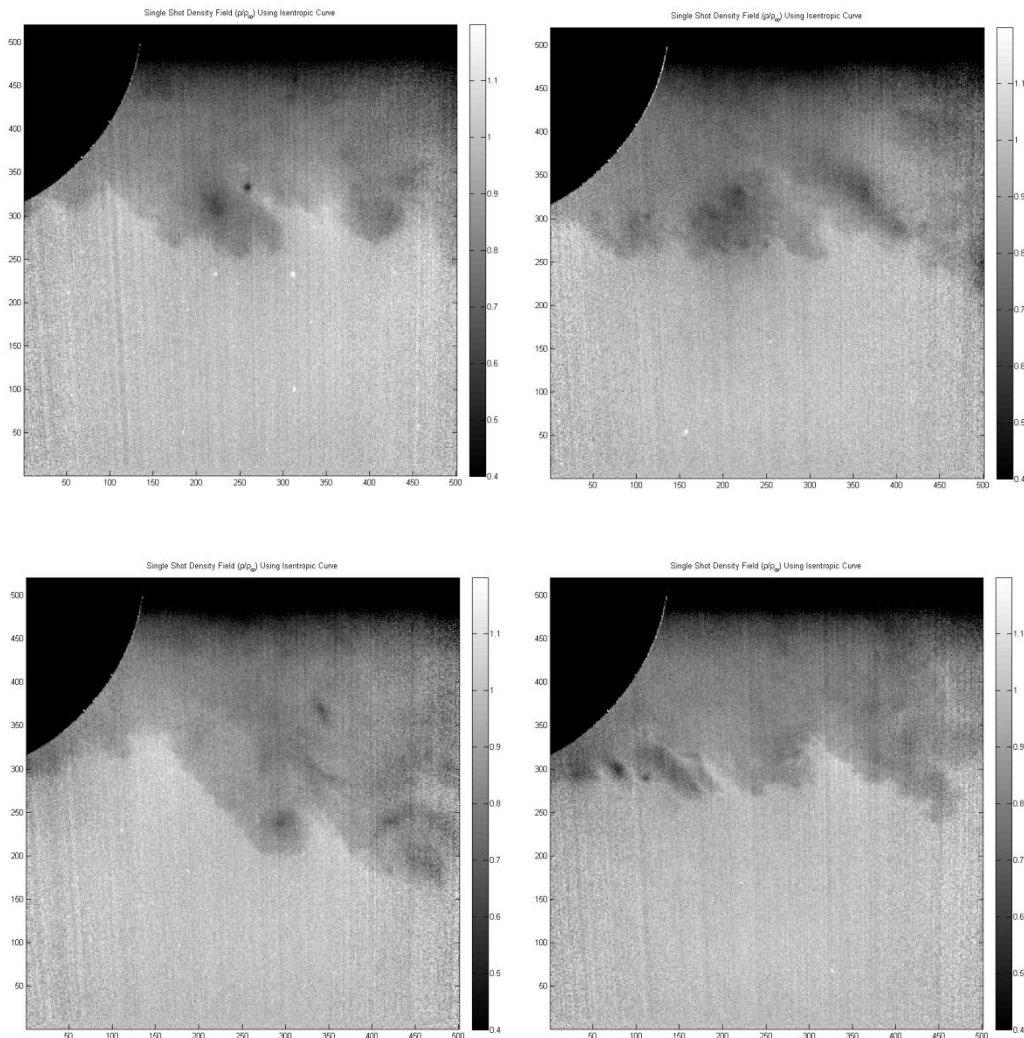


Figure 9: Single Shot Density Field Images Near Centerline

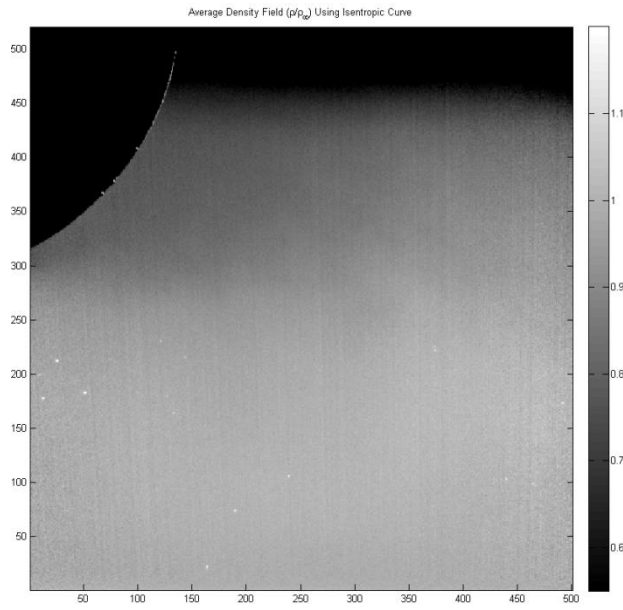


Figure 10: Average Density Image Near Centerline (70 images)

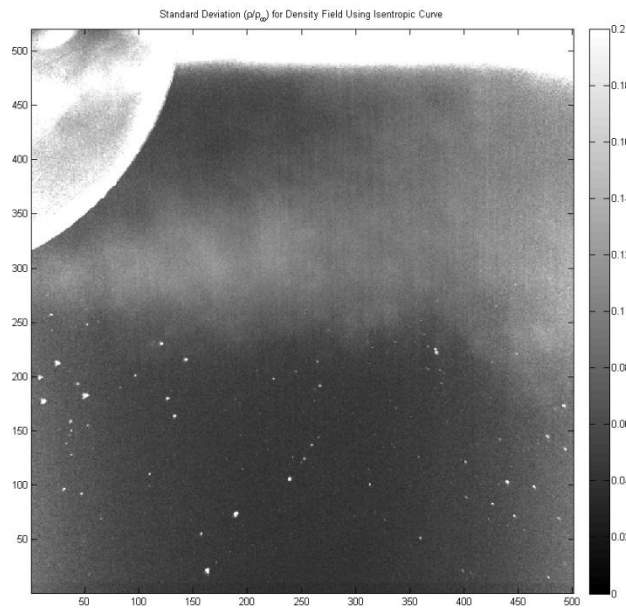


Figure 11: Standard Deviation of Density Images Near Centerline

C. Results from Time-Resolved Acetone PLIF Experiments

The time-resolved acetone PLIF experiments yielded inconclusive results. The signal levels in these images were low due to the limited laser energy of the pulse burst laser at 266 nm. Additionally, the noise characteristics of the Ultra68 camera prevented a useful signal-to-noise ratio from being obtained. There are still improvements that could provide more signal, including upgrades to the pulse burst laser and a new camera. It was concluded that if quality images could be obtained in these experiments, then experiments using the scanning technique could be easily carried out in the future.

Currently, the pulse burst laser system is being upgraded to include a more stable master oscillator and a sixth amplification stage, which are expected to increase the uniformity of each pulse and increase the energy generated at 266 nm by a factor of 3 or more, respectively. At the time of this writing, the upgraded components were not yet ready for use, but will be used in future studies. Also, two other high speed cameras are being considered for this work. A Princeton Scientific PSI-4 High Speed Camera is nearly ready to use. The large pixel pitch (115 μm) is better suited for signal-starved applications and should substantially increase the SNR of the measurement. Also, a variety of new high speed cameras are being investigated and may be acquired. In particular, the DRS Hadland Ultra24 and a Cordin 222-4G are being tested. These cameras both have lower noise characteristics and high resolution and should yield superior results compared to the Ultra68 camera.

V. Conclusion and Future Work

Advances have been made in the development of a high-speed 3-D density measurement technique using acetone PLIF. The turbulent wake region of a hemisphere at transonic conditions of approximately Mach 0.78 was investigated with acetone PLIF. The work presented here proved that high resolution, low image acquisition speed acetone PLIF images can be obtained for a high velocity, compressible flow (in this case the wake of a hemisphere which closely resembles the flow over a turret mounted to an aircraft) and density field data can be calculated. These single-shot acetone PLIF images showed that there are large density fluctuations in the shear layer and turbulent wake region and the maximum fluctuation from the freestream density is approximately 40-50%. This work also proved that time-resolved acetone PLIF images and their extension to 3-D scanning are not possible using the pulse burst laser system and the Ultra68 camera. PIV data was also obtained and analyzed to find the instantaneous velocity and vorticity fields. There are vorticity fluctuations in the turbulent wake region and the maximum velocity is seen to exist in the shear layer.

In the future, several changes will be made to the experimental setup that should increase the signal level of time-resolved acetone PLIF imaging. This will enable laser sheet scanning to be employed with a scanning mirror. A substantial upgrade in the pulse burst laser will be made combined with the use of new high speed cameras, which are expected to significantly improve the performance. In addition, PIV data will be obtained along multiple parallel planes in the flow field, so mean and fluctuating turbulent quantities can be calculated. This will better characterize the flow field and provide a comparison for acetone PLIF data.

Acknowledgements

This work was supported through an AFOSR Young Investigator Program Grant (FA9550-08-1-0150). The authors would like to thank Tim Fahringer for assistance during experiments and Andy Weldon for help with machining work. The authors would also like to thank The Ohio State University for current and future use of a Princeton Scientific PSI-4 high speed camera.

References

- ¹ Truman, C. R., and Lee, M. J., "Effects of Organized Turbulence Structure of the Phase distortion in a Coherent Optical Beam Propagating through a Turbulent Shear Flow," *Phys. Fluids*, Vol. 2, pp. 851-857, (1990).
- ² Hugo, R. J., Jumper, E.J., Havener, G., and Stepanek, C., "Time-resolved wave front measurements through a compressible free shear layer," *AIAA J.*, Vol. 35, No. 671 (1997)
- ³ Dimotakis, P. E., Catrakis, H. J., and Fourguette, D. C., "Flow Structure and Optical Beam Propagation in High-Reynolds-Number Gas-Phase Shear Layers and Jets," *J. Fluid Mech.*, Vol. 433, No. 105 (2001)
- ⁴ Yanta, W. J., Spring, W. C., Lafferty, J. F., Collier, A. S., Bell, R. L., Neal, D. R., Hamrick, D. R., Copland, R. J., Pezzanti, L., Banish, M., and Shaw, R., "Near- and Farfield Measurements of Aero-Optical Effects Due to Propagation Through Hypersonic Flows," AIAA Paper 2000-2357.
- ⁵ Thurow, B., Samimy, M., Lempert, W., Harris, S. R., Widiker, J., and Duncan, B., "Simultaneous MHz Rate Flow Visualization and Wavefront Sensing for Aero-optics," AIAA Paper 2003-0684.
- ⁶ Wyckham, C. M., Zaidi, S.H., Miles, R. B., and Smits, A. J., "Characterization of Optical Wavefront Distortion due to a Boundary Layer at Hypersonic Speeds," AIAA Paper 2003-4308.
- ⁷ Aguirre, R. C., Nathman, J. C., Garcia, P. J., and Catrakis, H. J., "Turbulent Refractive Fluid Interfaces and Aero-Optical Wavefront Distortions: Experiments and Computations," AIAA Paper 2005-1080.
- ⁸ Jumper, E. J., and Fitzgerald, E. J., "Recent advances in Aero-optics," *Prog. Aerospace Sci.*, Vol. 37, No. 299 (2001).
- ⁹ Fitzgerald, E. J. and Jumper, E. J., "The optical distortion mechanism in a nearly incompressible free shear layer," *J. Fluid Mech.*, Vol. 512, pp. 153-189, 2004.
- ¹⁰ Guezennec, Y. G., Brodkey, R. S., Trigui, J., and Kent, J. C. "Algorithms for fully automated three-dimensional particle tracking velocimetry," *Exp. Fluids*, Vol. 17, pp 209-219 (1994).
- ¹¹ Royer, H., "Holography and particle image velocimetry," *Meas. Sci. Technol.*, Vol. 8, pp. 1562-1572 (1997).
- ¹² Sheng, J., Malkiel, R., and Katz, J., "Single beam two-views holographic particle image velocimetry," *App. Optics*, Vol 42., pp. 235-250 (2003).
- ¹³ Elkins, C. J., Markl, M., Pelc., N., and Eaton, J. K., "4D Magnetic resonance velocimetry for mean velocity measurements in complex turbulent flows," *Exp. Fluids*, Vol. 34, pp. 494-503 (2003).
- ¹⁴ Thurow, B. S., and Lynch, K. P., "Development of a High-Speed Three-Dimensional Flow Visualization Technique," *AIAA Journal*, 47:2857-2865 (2009).
- ¹⁵ Catrakis, H. J., Garcia, P. J., and Nathman, J. C., "Cumulative Aero-Optical Interactions Along Laser Beam Propagation Paths: Experiments and Computations," AIAA Paper 2006-1495 (2006).
- ¹⁶ Lozano, A., Yip, B., and Hanson, R.K., "Acetone: a tracer for concentration measurements in gaseous flows by planar laser induced fluorescence," *Experiments in Fluids*, Vol. 13, pp. 369-376, 1992.

- ¹⁷ Thurber, Mark Clinton. "Acetone Laser-Induced Fluorescence for Temperature and Multiparameter Imaging in Gaseous Flows." Thermosciences Division Department of Mechanical Engineering Stanford University. Topical Report TSD-120. Stanford, CA. March 1999. February 2009.
- ¹⁸ Wernet, J. H., and Wernet, M. P., "Stabilized Alumina/Ethanol Colloidal Dispersion for Seeding High Temperature Air Flows," NASA Technical Memorandum 106591 (1994)
- ¹⁹ Wu, P., Lempert W., Miles, R., "Megahertz Pulse-Burst Laser and Visualization of Shock-Wave/Boundary-Layer Interaction," *AIAA Journal*, Vol. 38, pp. 672-679, 2000.
- ²⁰ B. Thurow, N. Jiang, M. Samimy, and W. Lempert, "Narrow-Linewidth Megahertz-Rate Pulse-Burst Laser for High-Speed Flow Diagnostics," *Applied Optics*, Vol. 43, pp. 5064-5073, 2004.
- ²¹ M. Wernet and A. Opalski, "Development and application of a MHz-frame rate PIV system," AIAA Paper 2004-2184 (2004).
- ²² A. Kastengren, J.C. Dutton and G. Elliott, "Time-Correlated Visualizations of Supersonic Blunt-Base Cylinder Wakes," AIAA Paper 2005-1346 (2005).
- ²³ Thurow, B., Satija, A., and Lynch, K., "3rd generation MHz rate pulse burst laser system," accepted for publication in *Applied Optics*, September 2008.
- ²⁴ Wernet, M. P., "Fuzzy logic enhanced digital PIV processing software," 18th Int. Congress on Instrumentation for Aerospace Simulation Facilities, (1999).